

OzDES Reverberation Mapping Program: Lag recovery reliability for 6-year C IV analysis

A. Penton^{1, *} U. Malik,² T. M. Davis,¹ P. Martini,^{3,4,5} Z. Yu,⁴ R. Sharp,² C. Lidman,^{6,2} B. E. Tucker,² J. K. Hoormann,¹ M. Agüena,^{7,8} S. Allam,⁹ J. Annis,⁹ J. Asorey,¹⁰ D. Bacon,¹¹ E. Bertin,^{12,13} S. Bhargava,¹⁴ D. Brooks,¹⁵ J. Calcino,¹ A. Carnero Rosell,¹⁶ D. Carollo,¹⁷ M. Carrasco Kind,^{18,19} J. Carretero,²⁰ M. Costanzi,^{21,22} L. N. da Costa,^{8,23} M. E. S. Pereira,²⁴ J. De Vicente,¹⁰ H. T. Diehl,⁹ T. F. Eifler,^{25,26} S. Everett,²⁷ I. Ferrero,²⁸ P. Fosalba,^{29,30} J. Frieman,^{9,31} J. García-Bellido,³² E. Gaztanaga,^{29,30} D. W. Gerdes,^{33,24} D. Gruen,^{34,35,36} R. A. Gruendl,^{18,19} J. Gschwend,^{8,23} G. Gutierrez,⁹ S. R. Hinton,¹ D. L. Hollowood,²⁷ K. Honscheid,^{3,37} D. J. James,³⁸ A. G. Kim,³⁹ K. Kuehn,^{40,41} N. Kuropatkin,⁹ M. A. G. Maia,^{8,23} J. L. Marshall,⁴² F. Menanteau,^{18,19} R. Miquel,^{43,20} R. Morgan,⁴⁴ A. Möller,⁴⁵ A. Palmese,^{9,31} F. Paz-Chinchón,^{18,46} A. A. Plazas,⁴⁷ A. K. Romer,¹⁴ E. Sanchez,¹⁰ V. Scarpine,⁹ D. Scolnic,⁴⁸ S. Serrano,^{29,30} M. Smith,⁴⁹ E. Suchyta,⁵⁰ M. E. C. Swanson,¹⁸ G. Tarle,²⁴ C. To,^{34,35,36} S. A. Uddin,⁵¹ T. N. Varga,^{52,53} W. Wester,⁹ and R.D. Wilkinson¹⁴ and (DES Collaboration)

Affiliations are listed at the end of the paper

Accepted XXX. Received YYY; in original form ZZZ

ABSTRACT

We present the statistical methods that have been developed to analyse the OzDES reverberation mapping sample. To perform this statistical analysis we have created a suite of customisable simulations that mimic the characteristics of each individual source in the OzDES sample. These characteristics include: the variability in the photometric and spectroscopic lightcurves, the measurement uncertainties and the observational cadence. By simulating six real sources that contain the C IV emission line, we developed a set of quality criteria that ranks the reliability of a recovered time lag depending on the agreement between different recovery methods, the magnitude of the uncertainties, and the rate at which false positives were found in the simulations. Of these six sources, two were given a quality rating of 1, corresponding to our ‘gold standard’. Lags were recovered at 223 ± 56 and 378 ± 104 days with redshifts of 1.93 and 2.74 respectively. Future work will apply these methods to the entire OzDES sample of ~ 750 AGN.

Key words: nuclei – galaxies: active – (*galaxies:*) quasars: supermassive black holes – (*galaxies:*) quasars: emission lines – quasars: general

1 INTRODUCTION

The innermost regions of active galactic nuclei (AGN) are powered by supermassive black holes, whose role in galaxy formation and evolution is complex and poorly understood. For AGN within the local Universe, high spatial resolution instruments are capable of probing the sphere of influence of the central black hole and directly measuring the mass (e.g., Gebhardt et al. 2000; Greene et al. 2010; Gebhardt et al. 2011; Kuo et al. 2011; Event Horizon Telescope Collaboration et al. 2019). However, we require alternate methods to study AGN at greater distances in order to explore the evolution of supermassive black holes. For this purpose, Reverberation Mapping (RM) can be used to directly measure distances within these

compact regions and infer the masses of the central supermassive black holes (SMBH).

The technique of Reverberation Mapping (Blandford & McKee 1982; Peterson 1993) uses time-domain observations to provide a window to AGN physics on spatial scales below the angular resolution of contemporary observatories. The prompt and variable rest-frame UV emission from the accretion disk ionises the more extended broad-line region (BLR). Variations in the UV continuum radiation from the disk produce a variation in the observed emission-line signal over an extended time scale, on the order of months to years. The observed reverberation of the BLR in response to the UV continuum is due to the light crossing time from the central source to the BLR and the geometry of the BLR. Therefore, by measuring this time delay, τ , we can measure of the radius of the BLR ($R_{\text{BLR}} = c\tau$). The velocity dispersion of the BLR (Δv) can

* E-mail: a.penton@uq.edu.au (UQ)

be estimated from the width of the broadened emission lines. The mass of the central black hole (M_{BH}) can then be measured using the Virial theorem:

$$M_{\text{BH}} = f \frac{R_{\text{BLR}} \Delta V^2}{G}, \quad (1)$$

where f is the virial coefficient; a dimensionless scale factor that accounts for the geometry, orientation, and kinematics of the BLR.

Extensive time-domain monitoring of both the continuum emission and emission line flux is required to conduct reverberation mapping of the BLR. Due to limits of technology at the time, early campaigns targeted few bright, highly-variable sources, which corresponded to relatively low-luminosity AGN in the local Universe. Subsequent generations of these surveys over many years gradually produced a sample of reliable lag measurements for 63 AGN (e.g., Kaspi et al. 2000; Onken & Peterson 2002; Peterson et al. 2004; Bentz et al. 2009b; Denney et al. 2010; Barth et al. 2011; Grier et al. 2012; Bentz & Katz 2015). As most of these sources were at low redshifts ($z < 0.3$), most results were obtained using the H β emission line. The observations confirmed the predicted relationship between the AGN luminosity and the radius of the BLR (Kaspi et al. 2000; Bentz et al. 2006; Bentz et al. 2009a).

This Radius-Luminosity ($R-L$) relationship is a powerful tool to estimate SMBH masses from a single-epoch spectroscopic measurement. This has allowed single-epoch Virial BH mass estimates to be made for tens of thousands of objects (Shen et al. 2011), in order to study SMBH evolution. However, for sources at higher redshifts (and hence greater evolutionary lookback times), H β is redshifted into the near-infrared spectrum and becomes increasingly challenging to observe. For these more distant sources, both single-epoch and RM observations rely on emission from Mg II and C IV, for which a detailed $R-L$ relation calibration is not yet available. This inhibits the direct construction of single-epoch virial BH estimates for these important sources. Single-epoch SMBH mass estimates based on Mg II and C IV are calibrated based on UV spectra of local sources (Vestergaard & Peterson 2006).

These AGN have longer lags, due to both the increased intrinsic luminosity of the observed sources, and the impact of time dilation, thus requiring long-baseline monitoring. With the C IV line, significant RM measurements have been made for an additional 65 AGN to date (Peterson et al. 2004, 2005; Metzroth et al. 2006; Kaspi et al. 2007; Trevese et al. 2014; Lira et al. 2018; Hoormann et al. 2019; Grier et al. 2019; Shen et al. 2019).

Recent ‘industrial-scale’ Reverberation Mapping campaigns have probed new regions of the AGN luminosity-redshift parameter space, with a particular focus on high-redshift sources. The Australian Dark Energy Survey (OzDES see (Yuan et al. 2015; Childress et al. 2017)) began one of the first multi-object RM campaigns, monitoring 771 AGN over a 6-year baseline with the Anglo-Australian Telescope. This was complimented by photometric monitoring of the same sources in the Dark Energy Survey (DES see (Dark Energy Survey Collaboration et al. 2016)) deep fields for the same time period. With the ability to conduct multi-object spectroscopy, OzDES was able to target hundreds of AGN over a broad range of redshifts ($0.1 < z < 4.5$) and luminosity (apparent r -band AB magnitudes from $17 < r < 22.5$). About one-third of these AGN are at redshifts greater than 1.7, where the C IV line is visible. Hoormann et al. (2019) published our first RM results with the C IV line, for two sources at redshifts of 1.905 and 2.593, which are among the highest redshift and highest mass black holes measured to date with RM.

Due to our goal of measuring these high-redshift long-duration

AGN time-lags, the observational window of our survey differed from traditional RM programs that employ single-object spectrographs. A multi-year baseline was required to ensure the longer lags could be measured. As the spectroscopic counterpart of the Dark Energy Survey, we monitored the supernova fields (Neilsen et al. 2019), which were visible for ~ 6 months of the year. We used a lower cadence for the spectroscopic monitoring than traditional surveys. Monthly monitoring of an AGN at $z \sim 3$ is approximately equivalent to weekly monitoring of an AGN at $z \sim 0.1$ because of the factor of ~ 4 in time dilation. A similar industrial-scale survey was conducted by the Sloan Digital Sky Survey Reverberation Mapping Project (SDSS-RM) (Shen et al. 2015). Simulations for the OzDES RM and SDSS-RM programs (King et al. 2015; Shen et al. 2015) and recent RM results from these programs (Hoormann et al. 2019; Grier et al. 2019; Grier et al. 2017; Homayouni et al. 2020) show how the observational window presents challenges for recovery of these high- z AGN lags, such as aliasing due to seasonal gaps. In addition, lag recovery depends on the signal-to-noise of the flux measurements and observed intrinsic continuum variability of the AGN. We were motivated to develop more sophisticated statistical techniques by the complications of seasonal gaps, changes of cadence, and variations in S/N of both the continuum and emission line data.

The most widely used lag recovery methods in the literature are the Interpolated Cross-Correlation Function (ICCF), (Gaskell & Peterson 1987) and JAVELIN (Zu et al. 2011). These techniques have proven to recover reliable and consistent lags for traditional RM surveys, however this has not conclusively been shown for large-scale RM programs targeting higher- z AGN. The restricted signal-to-noise and more limited sampling of these programs dictate a rigorous analysis of the biases and false positive rates, to devise robust lag recovery and confidence criteria. Two comprehensive studies comparing lag recovery methods have been performed recently. Simulations conducted by Li et al. (2019), specifically for SDSS-RM, found JAVELIN performed better overall than ICCF, but were performed with preset detection criteria on populations of sources, rather than the individually customised simulations that will be used here to inform our significance criteria. These results were corroborated by Yu et al. (2020), who found JAVELIN produced more correct lag uncertainties, however their results were based off simulated light curves of a few local sources that had been monitored at very high cadence.

In this work, we conduct simulations using mock light curves representative of our data quality, created on a source-by-source basis, to compare the performance of these lag recovery techniques. This is used to determine the recovery and significance criteria that will be used for following OzDES RM analyses with each emission line. To test the methods and statistics for this sample we have chosen a set of six sources (shown in Figure 1) that cover a range of quality and properties as shown in Table 1. A small number was chosen due to the high level of computational resources required to undertake this testing. Using a small number of sources also allows us to test the analysis methods to be then applied to the entire OzDES sample. To choose these sources we used the variability measure from Fausnaugh et al. (2016) as a proxy for signal-to-noise in the lightcurves, with these sources having variability that spans the whole sample. We also use the expected lag for the source based on the present radius-luminosity relations (Bentz et al. 2009a; Trakhtenbrot & Netzer 2012; Kaspi et al. 2007). This is due to the expected recoverability of certain lags and the need for a representative variety of sources.

Section 2 describes the model used to create our simulated

Table 1. The characteristics of the six sources used in this analysis. Sources with a wide array of redshifts (1.9-3.5) and variabilities were chosen in an effort to find a representative sample. There is also a wide variety of predicted lags both in the measured frame and the rest frame (adjusted for cosmological time dilation.)

DES ID	Name	Redshift	Variability	R-L predicted observed frame lag (days)
DES J022514.52-044700.1	J0225-0447	1.93	0.09	218
DES J032923.28-280022.7	J0329-2800	2.18	0.05	189
DES J025102.16-004142.8	J0251-0041	2.43	0.19	98
DES J034121.48-265901.0	J0341-2659	2.62	0.25	316
DES J022620.76-045946.5	J0226-0459	2.74	0.05	144
DES J034122.56-291302.0	J0341-2913	3.47	0.11	344

AGN light curves. The lag recovery methods and structure of our simulations are discussed in Section 3. The results of these simulations are presented in Section 4, and applied to observed data in Section 5. We summarise our results and outlook to the future in Section 6.

2 SIMULATIONS

In this work we aim to create simulations that are specially made to represent each individual source in our sample. This is in contrast to previous works ((Li et al. 2019)) that have considered behaviours of large samples by creating a large variety of mock sources within their observational parameter space. However, the AGN variability models that are utilised are the same. Kelly et al. (2009) showed that a damped random walk (DRW) can be used to model the stochastic variability of AGN light curves. A DRW is a random walk with an additional term that pushes deviations back to the mean value. This model is characterised by two parameters, the damping timescale and the amplitude, which are unique to the source. Kozłowski et al. (2010) and MacLeod et al. (2010) extended this work and compared this model to more observed AGN light curves, applying the DRW model to more AGN light curves to directly constrain the variability parameters. MacLeod et al. (2010) determined the correlations between the variability parameters and physical AGN properties, including luminosity and black hole mass, using photometric light curves for ~8,000 spectroscopically confirmed quasars in the Stripe 82 field, which were monitored over a 10 year baseline by the Sloan Digital Sky Survey (SDSS).

We simulate light curves following the method described by King et al. (2015), which is the same DRW model used by Kelly et al. (2009), Kozłowski et al. (2010), and MacLeod et al. (2010), applied specifically for each of the objects in the OzDES RM program. The continuum and emission-line light curves are created as described in the Section 2.1. Following this, we describe the customisation for each source, and the simulation set-up used for our analysis.

2.1 Continuum and emission-line light curves

The following parameters are required to model the continuum and emission-line light curves for an AGN:

- mean of the lightcurve, μ ;
- damping timescale, τ_D , in days;
- long-term structure function, SF_∞ , in mag;
- lag, τ , in days.

The damping timescale (also referred to as the relaxation time or characteristic time-scale) is the average time it takes for the random walk to return to the mean. The amplitude of the DRW can be

described a function of the standard deviation of the DRW known as the structure function, $SF(\Delta t)$. The simulated light curves for the OzDES AGN sample need to be generated for a survey baseline of at least $\Delta t = 7$ years. The asymptotic value of the structure function at large Δt is:

$$SF(\Delta t \gg \tau_D) \equiv SF_\infty = \sqrt{2}\sigma \quad (2)$$

where σ is the long-term standard deviation of the variability.

The continuum lightcurve, in magnitudes, is defined by a damped random walk with a mean μ , and variable term $\Delta C(t)$:

$$C(t) = \mu + \Delta C(t) \quad (3)$$

where μ is the monochromatic continuum flux density at a given wavelength, converted to an apparent magnitude. The variable term at $t = 0$ is $\Delta C(t_0) = \sigma G(1)$, where σ is as defined in Equation 2, and $G(1)$ is a random number drawn from a Gaussian distribution with a mean of 0 and standard deviation of 1. Subsequent variable terms are given by:

$$\Delta C(t_{i+1}) = \Delta C(t_i) \exp\left(\frac{-|t_{i+1} - t_i|}{\tau_D}\right) \quad (4)$$

$$+ \sigma G(1) \left[1 - \exp\left(\frac{-2|t_{i+1} - t_i|}{\tau_D}\right)\right]^{\frac{1}{2}}. \quad (5)$$

Blandford & McKee (1982) interpret the emission-line flux variations as a response to continuum variations using:

$$\Delta L(t) = \int \Psi(\tau) \Delta C(t - \tau) d\tau, \quad (6)$$

where $\Delta L(t)$ is the emission-line light-curve flux relative to its mean value, $\Psi(\tau)$ is the transfer function, $C(t)$ is the variable component of the continuum lightcurve flux and τ is the lag. The transfer function describes the BLR emission-line flux response to a delta function variation of the continuum flux. It has the effect of smoothing the emission-line lightcurve and shifting it, relative to the continuum lightcurve, by the lag τ . We convolve the continuum lightcurve with a top-hat transfer function to generate the smoothed and shifted emission-line lightcurve. As the true form of $\Psi(\tau)$ is complex and related to the geometry and kinematics of the BLR (Peterson 2001), we use the top-hat as an approximation. As in Zu et al. (2011), we use a top-hat transfer function of the form:

$$\Psi(t) = \begin{cases} \frac{1}{w} & \tau - w/2 < t < \tau + w/2, \\ 0 & \text{otherwise} \end{cases}, \quad (7)$$

where w is the width of the top-hat. Following King et al. (2015) we adopt $w = 0.1\tau$.

To generate light curves for the AGN sample monitored by

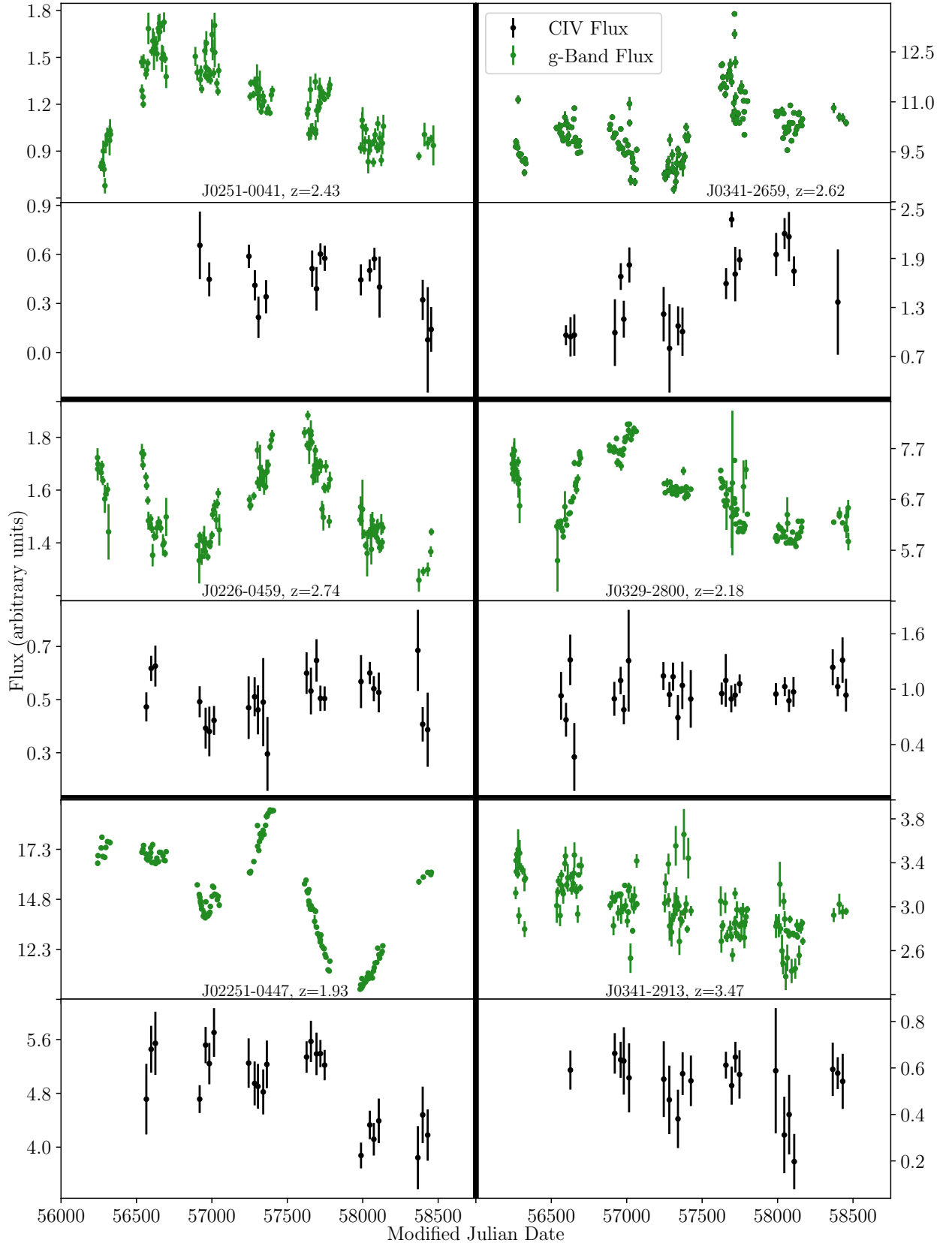


Figure 1. Lightcurves for all six sources. CIV emission line lightcurves shown in black, with g-band photometric lightcurves shown in green. The photometric lightcurves contain 7 seasons of data with approximately weekly cadence. These are accompanied by spectroscopic lightcurves containing 5-6 seasons of approximately monthly cadence.

Table 2. Definitions for different times lags to be used in the following analysis.

Symbol	Description
τ_{expected}	Expected time lag for data (based on luminosity)
$\tau_{\text{data,meas}}$	Measured time lag from real data
τ_{sim}	Simulated time lag
$\tau_{\text{sim,control}}$	Simulated time lag at $\tau_{\text{data,meas}}$
$\tau_{\text{sim},x}$	Simulated time lag at $x \times \tau_{\text{data,meas}}$
$\tau_{\text{sim},x,\text{meas}}$	Measured time lag using simulated data at $x \times \tau_{\text{data,meas}}$

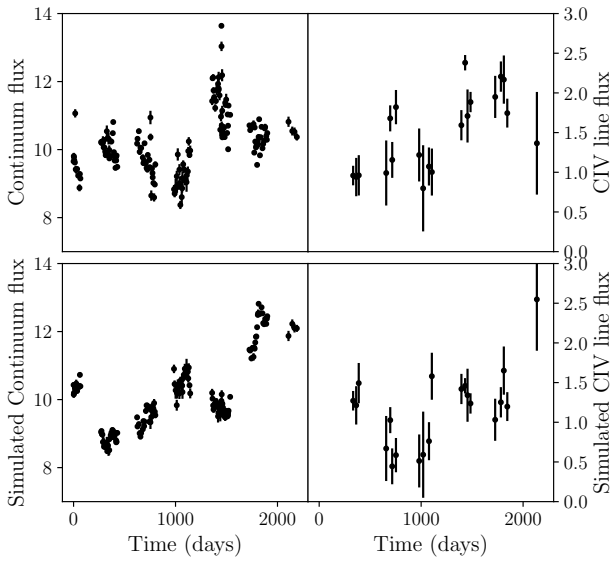


Figure 2. Comparison of simulated continuum and emission line lightcurves (top) to observed continuum and emission line lightcurves (bottom). Note that whilst they are inherently different, the uncertainties, cadence, mean and variability are consistent between the top and bottom panels.

the OzDES RM program, the four parameters described above (μ , τ , τ_D , SF_∞) were used to create a bespoke simulation for each source. The parameters were found using the apparent r -band AB magnitudes and redshifts unique to each source, as described in Appendix A. The light curves are also scaled such that their magnitudes and variations are consistent with the lightcurve of the source from which they are modelled (‘parent’ source).

2.2 Cadence and uncertainties

Our custom simulations have the same cadence and noise properties as the data for each AGN. We construct them by producing high cadence lightcurves using the method illustrated in the previous sections. These are then subsampled to have identical cadence as their ‘parent’ source. This ensures that any effects that are a function of the observational window are reflected in the simulations. In addition to this, the absolute errors from the parent source are used directly. This ensures that the simulated lightcurves include any observational effects caused by the survey. The final result of this process is shown in Figure 2.

2.3 Matching simulations to data variability

During development it was found that, due to the sub-sampling, the difference in variability of different realisations could vary con-

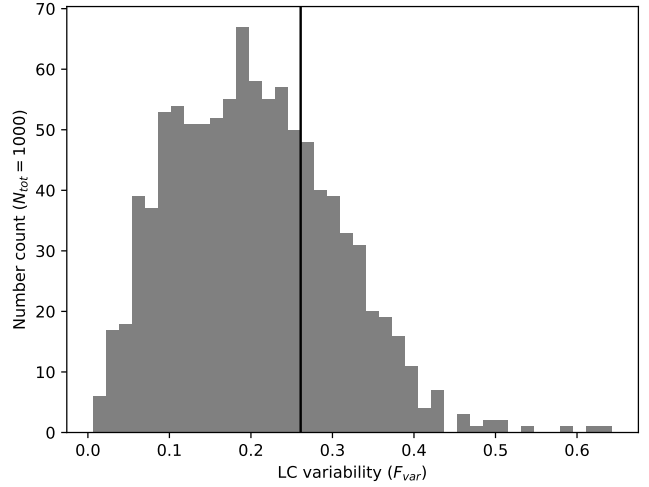


Figure 3. Variability of 1000 subsamples of the same underlying lightcurve. This shows the dispersion in the apparent variability from subsampling a simulation to match the observing cadence. The black vertical line indicates the measured variability of the parent source.

siderably by chance. This can be shown by subsampling the same underlying lightcurve with the same cadence but with different starting points. The distributions of variability are shown in Figure 3. Since it is likely that lightcurve variability is an important parameter in the recoverability of a time lag, it is vital that this is representative in the simulations.

To ensure that the simulated lightcurves closely match the data we perform a post-selection based on the lightcurve variability. Performing the post-selection is done by retaining the photometric-spectroscopic pair of lightcurves only if the measured variability after subsampling is within 33% of the observed variability of the input source. In this case the variability is quantified to be the fractional variability F_{var} (Fausnaugh et al. 2016) to encapsulate the variation of the lightcurve inclusive of errors,

$$F_{\text{var}} = \frac{1}{\langle f(t) \rangle} \sqrt{\frac{1}{N} \sum_i^N \{ [f(t_i) - \langle f(t) \rangle]^2 - \sigma_i^2 \}}. \quad (8)$$

Where $f(t_i)$ are flux values in the lightcurve and σ_i are the errors on each data point. This subsampling process also allows us to allow some freedom in our input parameters, importantly the BH mass. Assuming a specific black hole mass would likely bias the simulations as the black hole mass is not accurately known. Therefore, for each simulated lightcurve a new black hole mass is drawn from the parent distribution (Figure A1). This allows some realisations to have a high black hole mass, and therefore a high intrinsic variability, while others have low black hole mass and a low intrinsic variability. Both can appear to have the same variability after subsampling based on observational cadence and this method allows us to not be biased to any specific black hole mass based on variability.

2.4 Range of time-lags simulated

More luminous AGN tend to have longer time-lags. One can use the $R-L$ relation to predict the time-lag (τ_{expected}) for a source based on its absolute luminosity. However, for each of the sources that is used

in this analysis, a range of different lags has been considered. This means that not only were the sources simulated with the expected time delay but with a range of eight time delays ranging from 20% of τ_{expected} to 160% of τ_{expected} (see Table 2), giving eight sets of simulations for each source, each containing 200 lightcurves, all of which pass the variability selection discussed in the previous section, giving a total of 1600 simulations per source. This was done in an attempt to not bias our analysis towards recovering lags that were exactly what were expected.

3 LAG RECOVERY METHODS

Two of the most commonly used lag recovery methods are the Interpolated cross-correlation function (ICCF) (Gaskell & Peterson 1987; Peterson et al. 1998) and JAVELIN (Zu et al. 2011, 2013). The Interpolated Cross-Correlation Function (ICCF) uses linear interpolation to provide information about the lightcurve between data points. Under the assumption of smooth variations in lightcurve structure on intermediate time-scales, linear interpolation of the observational data sets maps the sparse sampled photometric and spectroscopic light curves to a common sampling frequency prior to cross-correlation. The statistical and systematic uncertainties in the cross correlation are estimated via bootstrap sampling (Gaskell & Peterson 1987; Peterson et al. 1998).

Employing a more sophisticated statistical model, JAVELIN employs a Markov chain Monte Carlo (MCMC) approach based on a Damped Random Walk (Section 2) for AGN variability. This is then used to constrain the time lag between lightcurves. While both ICCF and JAVELIN will be considered and employed in this analysis, the final results will utilise JAVELIN results.

A third contemporary lag recovery methodology, CREAM (Starkey et al. 2016), uses modelling of the thermal emission from the regions around the host black hole to constrain the time lag, however this method is not considered in this analysis at this time.

3.1 Lag Posterior Analysis

From both JAVELIN and ICCF lag recovery methods the output is a probability distribution function (PDF) of possible lags as seen in Figure 4. There are multiple ways that a time lag and uncertainty can be computed from the PDF. The choice of how to compute a lag and uncertainty is important as it can vastly affect the result.

The criteria that we used to determine the best method were:

- $\Delta\tau$: the absolute offset of the recovered time lag from the input time lag, and
- χ_{red}^2 : the reduced χ^2 between the recovered time lag and the input time lag.

These should yield $\Delta\tau = 0$ and $\chi_{\text{red}}^2 = 1$ if the lag and uncertainties are perfectly representative.

We considered three methods to determine the most representative way to determine the lag: the mean, the median and the peak of the PDF. We also considered three methods to compute the uncertainty: the mean absolute deviation (Mean AD), the median absolute deviation (Median AD), and the area that encloses 32% (1σ) of the probability on each side of the preferred lag (Count Out) as is used by default in JAVELIN. These methods were then applied to the PDFs from JAVELIN and ICCF for 100 simulated lightcurves for each of the sources and for eight different lags as discussed in Section 2.4. Note that the the PDFs for both JAVELIN

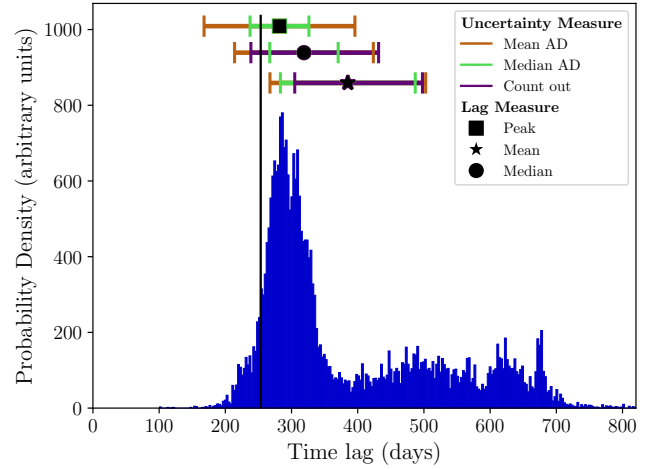


Figure 4. Example of the output PDF from JAVELIN with best fits and error bars shown using different methods of recovering lags and uncertainties. The three distinct groups represent three different ways of measuring the lag itself: the peak, the mean, and the median of the PDF. The colours in each set show the errorbars associated with using the different methods of measuring uncertainty: the mean absolute deviation, the median absolute deviation, and Count Out which employs 32% of the probability on either side of the lag. The black vertical line marks the input lag of the simulation. Note: there is no Count Out option for the peak lag recovery method as the method often failed in noisy PDFs.

and ICCF have a bin width of 3 days, this was this was found to be the smallest bin size that made the PDFs smooth enough to accurately define the peak.

Figure 5 compares the $\Delta\tau$ and χ^2 from the three different methods for computing the lag and uncertainties. From this we conclude that the mean is the worst estimator of time lag. This is likely due to poorly constrained lags having means that are central to the prior range. Since in this case the prior range is three times the input lag, the mean estimate will often skew upwards since the center of the prior range is greater than then input lag. This skew will get more severe at longer time lags as the difference between the input lag (τ_{control}) and the center of the prior range ($1.5\tau_{\text{control}}$) get larger with larger τ_{control} . There is little difference between the median and the peak of the distribution; more information will be required to conclude which is better including whether or not one is more biased. This will be discussed later in this section.

As far as using the correct uncertainties, we prefer a method that formally overestimates the uncertainties rather than underestimates them. This is because there are likely unmodelled systematics due to the complexity of the AGN such as a complex kinematics and the observational window function. Marginally overestimating our errorbars is more likely to be representative of the true uncertainty on the measurements. Thus we can immediately discount using the ‘Count Out’ method, seen in purple, as this gives significantly underestimated error bars, shown by having $\chi_{\text{red}}^2 > 1$ for all lags. Since we have already discounted using the mean of the distribution and using the median absolute deviation gives $\chi_{\text{red}}^2 > 1$ for almost all lags, as seen in green, we will be using the mean absolute deviation shown in Figure 5 in orange as our uncertainty measure.

We have considered the effect of prior range to decide between the two remaining possibilities for the best lag value (median or peak). In the previous tests shown in Figure 5 the baseline for

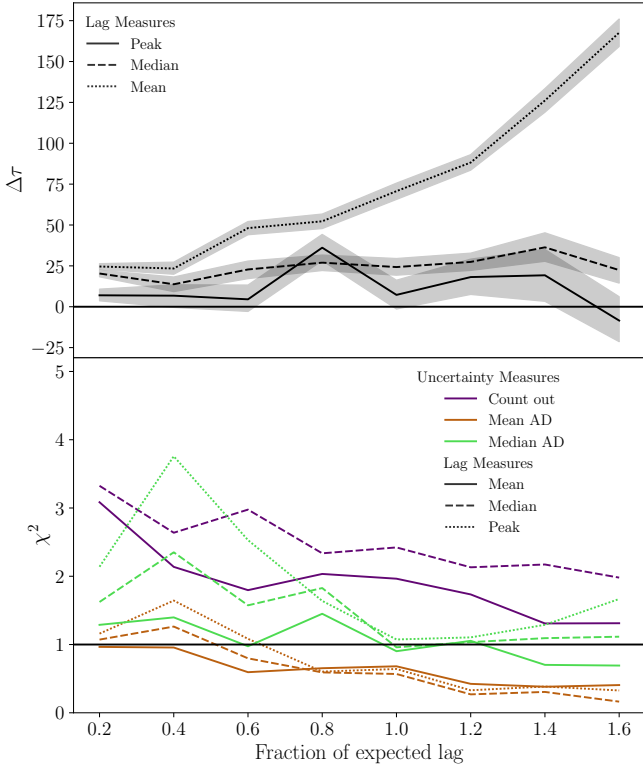


Figure 5. Example of the effectiveness of the different lag recovery and uncertainty methods. The black horizontal lines represent the desired values that would represent the optimal lag measure and uncertainties. The top panel shows that the peak and the median are on average the best lag measures, though both display a consistent positive offset from the true lags. This is likely due to the prior range that is used in these recoveries ($3\tau_{\text{sim},x}$ for each lag fraction x), which is asymmetric about the true lag. This means that for poorly constrained recoveries there is more probability space above the true lag giving comparatively more weight to the regions above the lag than below. The bottom panel gives a clear indication that the mean absolute deviation is the best uncertainty determinant as the other options consistently underestimate the uncertainties. This is shown by having a $\chi^2_{\text{red}} > 1$ consistently.

each simulation was three times the input lag for that simulation. However, when we analyse our data, we do not want the choice of prior range to strongly affect the recovered lag. To test which of these recovery methods is the least sensitive to prior range, for each source we analysed the simulated data with JAVELIN using a single prior of $3 \times \tau_{\text{sim}}$ (see Table 2). This is in contrast to the previous analysis, which used a prior of $3 \times \tau_{\text{sim},x}$, and this changed for each different input lag.

Figure 6 further illustrates how the mean (shown in blue) is the most biased of all of the methods, showing a consistent and steep trend. There is little difference between using the peak (red) and the median (green) as far as the lag itself. However, when we consider the χ^2_{red} test the mean absolute deviation (dark red) is the least biased. Using this method results in the combination of most accurate lag measure and consistent error bar size, shown by the χ^2_{red} being consistently close to one but slightly below, meaning that if anything we are marginally overestimating the size of our errors. From this analysis we concluded that when we quote a value for the lag we will use the peak of the distribution as the lag value, and the mean absolute deviation as the uncertainty.

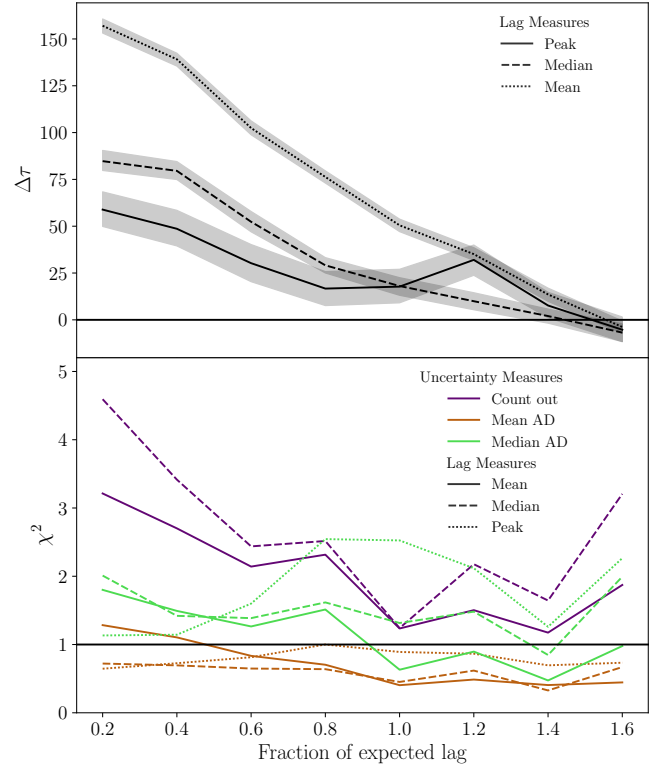


Figure 6. Example of the effectiveness of the different lag recovery and uncertainty methods given a constant prior range. In this case we used a fixed prior range of $3\tau_{\text{sim},1.0}$ for all input lags as opposed to varying $3\tau_{\text{sim},x}$ as in Figure 5, which is different for the different input lags. Running the analysis with a common baseline shows an indication of the systematic bias that arises from the choice of prior range. The bottom panel confirms that the mean absolute deviation will give the most representative uncertainties. The top panel shows that the peak gives the least systematically biased lag measure and will therefore be used for the rest of this analysis.

3.2 Non-Gaussianity, using the whole PDF

Throughout this analysis we observed that the lag PDFs were generally non-Gaussian, as illustrated by Figure 4. This implies that irrespective of the method that we chose to determine the lag and uncertainty, Gaussian errors would misrepresent the total probability. Due to this it seems that it would be beneficial to use the whole lag posterior when possible, such as when generating the $R-L$ relation. This would, in theory, give more information of the complex nature of the lag probability posterior. We test whether or not using this extra information yields more representative results by fitting a straight line to the recovered lag from our simulations as a function of the expected lag (the lag input into the simulations). We fit the straight line based on (a) the full PDFs and (b) just the peaks of the distributions. In both cases this should yield a linear fit with an intercept of 0 and a slope that is equal to the time lag of the control lag fraction ($1.0 \times \tau$).

The result is shown in Figure 7, which shows that the complete PDFs tend to have more power at longer lags than is physical. This manifests itself as a fit that gives not only a positive offset compared to the ‘true’ fit, but also a steeper slope in general. This trend was consistent across all tests, leading to the conclusion that whilst one might expect that using the full PDFs would provide a

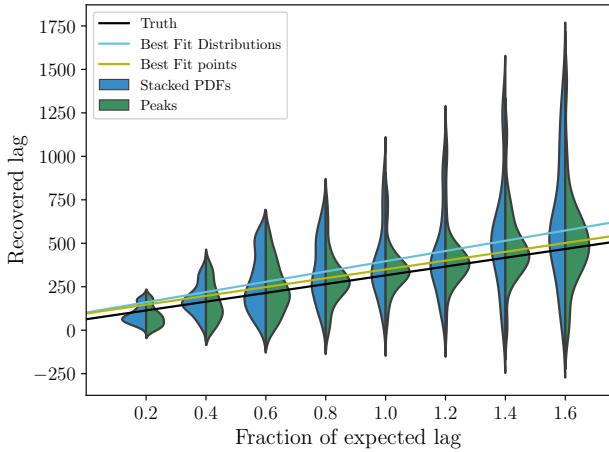


Figure 7. Simulation of the impact of fitting with the full posterior versus summary statistics. The blue distributions are a representative subsample of 100 stacked PDFs for each lag fraction, and the green distribution is the distribution of the peaks of the aforementioned PDFs. The black line represents the expected fit given the simulation inputs. The parent source for these simulations was J0341-2659, which has an expected lag of 316 days.

more statistically complete picture of the lags, it does not seem to properly reflect the ‘truth’ due to the existence of spurious signals in the PDFs.

This test also confirms what was observed in Figure 5, there was a consistent positive offset at all lag fractions. The slight positive offset in the “*Best Fit points*” result in Figure 7 is consistent with the tendency to overestimate the average recovered lags seen in Figure 5. This result is dominated by low signal-to-noise fits for which the lag is weakly recovered, so the prior affects the result. Recall we test lags from $0 < \tau < 3.0\tau_{\text{expected}}$, and the asymmetry in that prior causes more power to exist above the true lag than below.

4 CRITERIA TO ESTABLISH LAG MEASUREMENTS

Understanding the systematic versus statistical uncertainties in the recovered reverberation lags is critical for the use of AGN for cosmology. The complex nature of the interaction between the intrinsic source properties, time dilation effects due to redshift, the observational window functions and the underlying observational errors on these data sets mean that evaluation of the true confidence interval on any given lag recovery requires detailed analysis.

4.1 First quality cut - systematic error rejection

Our simulation data set indicates that both ICCF and JAVELIN are systematically biased to higher $\Delta\tau$ recoveries on average when used independently (see Figure 8). For ICCF this is an artifact of increased noise when compared with JAVELIN (due to the less optimal interpolation scheme). While JAVELIN makes use of a more sophisticated interpolation, it appears to be more susceptible to identifying longer lags due to aliasing effects from the seasonal gaps.

Figure 8 shows the $\Delta\tau$ for each method independently as dashed lines, and also for the sub sample in which we only use sources for which both methods provide a lag constant to within 1σ as defined in Equations 9 and 10. We find that for sources where both methods

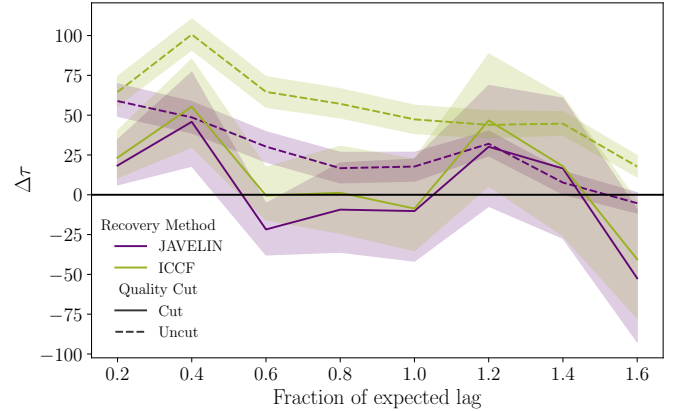


Figure 8. Improvement that results from requiring ICCF and JAVELIN to agree within 1σ . The combination of JAVELIN and ICCF improves accuracy on average. There is also a reduction in the positive offset in the uncut sample, with some of the lag bins recovering a small negative offset.

agree the distribution of errors in $\Delta\tau$ is reduced and symmetric around 0.

We define consistency between ICCF and JAVELIN as:

$$\tau_{\text{jav}} - \sigma_{\text{jav}} < \tau_{\text{iccf}} < \tau_{\text{jav}} + \sigma_{\text{jav}} \quad (9)$$

or:

$$\tau_{\text{iccf}} - \sigma_{\text{iccf}} < \tau_{\text{jav}} < \tau_{\text{iccf}} + \sigma_{\text{iccf}} \quad (10)$$

The purpose of this comparison cut is to eliminate cases where one method detects a spurious signal. The same spurious signal may not be detected by both methods, therefore we expect to see more consistent and accurate results when using the combination thereof. In Figure 8 we can see that on average, the cuts result in a more accurate representation across the lag fractions. There are cases where either JAVELIN or ICCF does better before the cuts, however, the cuts provide a more consistent result. This type of stability and reliability will be key when it comes to processing the complete OzDES sample.

4.2 Second quality cut - statistically error rejection

We also require recoveries to not agree with a time lag of zero within a 3σ confidence bound. When there is either a very weak or non-existent signal in the data, the common result is a very broad PDF. This causes very large error bars in most cases, and this would increase the likelihood that JAVELIN and ICCF would agree simply due to the size of the uncertainties and not due to the consistency in the signals. In most cases such weak signals would be consistent with zero at the 3σ level and therefore will be removed by this cut.

To ensure that only the simulations that would result in a successful lag recovery in the observed data are used when considering statistics such as false positive rate, we perform the same cuts on the simulations as we discussed for the observed lightcurves. Figure 9 shows the results of performing these cuts on 3500 simulations, with the black points having passed these cuts and red and blue having failed the first and second cuts respectively. From this it is already evident that if this source were to contain a lag of < 150 days, the lag would most likely not be confidently measured. This is likely due the variation timescale and observing cadence of the source. This point is made even clearer in Figure 10. Approximately 90% of the

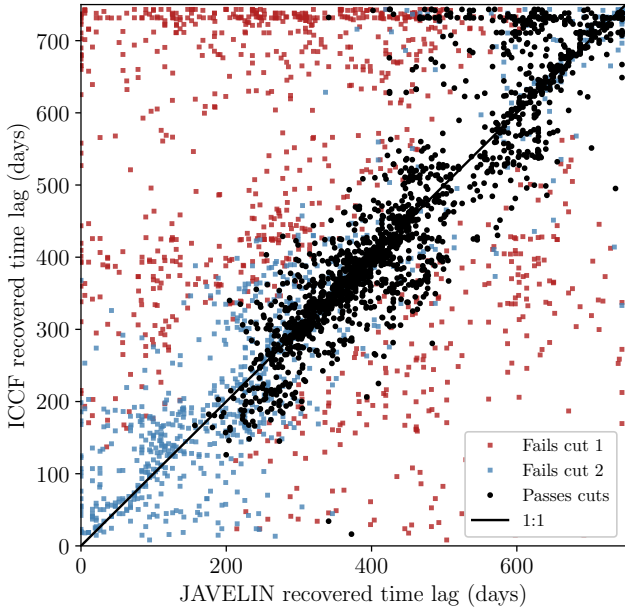


Figure 9. Lag recoveries for all 3500 simulations for J0226-0459. The simulations where JAVELIN and ICDF did not recover the same lag are highlighted in red, those where the uncertainty exceed 33% are in blue and those that passed both of these cuts are shown in black.

simulations with a lag of ~ 150 days failed the cuts as well as approximately 75% of those at ~ 225 days. This indicates the specific observing cadence and data quality of these sources is ineffective in recovering lags of that length. For all of the other lags at least 50% of the simulated light curves pass both cuts. This acceptance fraction is expected as the imperfect cadence and signal-to-noise in the light curves limits the quality of the sample as a whole.

4.3 False positive rates

In order to assess the efficacy of the applied quality cuts, we compare the recovered lag estimates for simulated sources to the input simulation lag. This comparison, showed in Figure 11 shows that, even after the first two cuts have been applied, there is still a significant portion of the simulations that measure incorrect lags.

As final quality measure we will define a false positive rate. For any given measured lag value, we define the false positive rate (FPR) as the fraction of sources, drawn from across the full range of simulated input lags, that erroneously present as the measured lag with high confidence. Measuring this quantity will enable us to remove sources that include a systematic error in the time lag signal, for example a signal that arises from aliasing due to the observing cadence.

Figure 12 graphically shows how we compute the FPR. The black points show the simulations where the recovered lag is within 1σ of the lag that was recovered in the observed lightcurve. Of these, we find the instances where a source recovers a lag consistent with that measured in the observed data but the recovered lag disagrees with its input beyond a 3σ level, these are presented in blue. This is important as, given Gaussian errors, we would only expect 1% to be inconsistent at this level. In the case pictured, the red points make up $\sim 5\%$ of the coloured points, this means that having recovered a lag of ~ 400 days there is a $\sim 5\%$ chance that your recovery passes

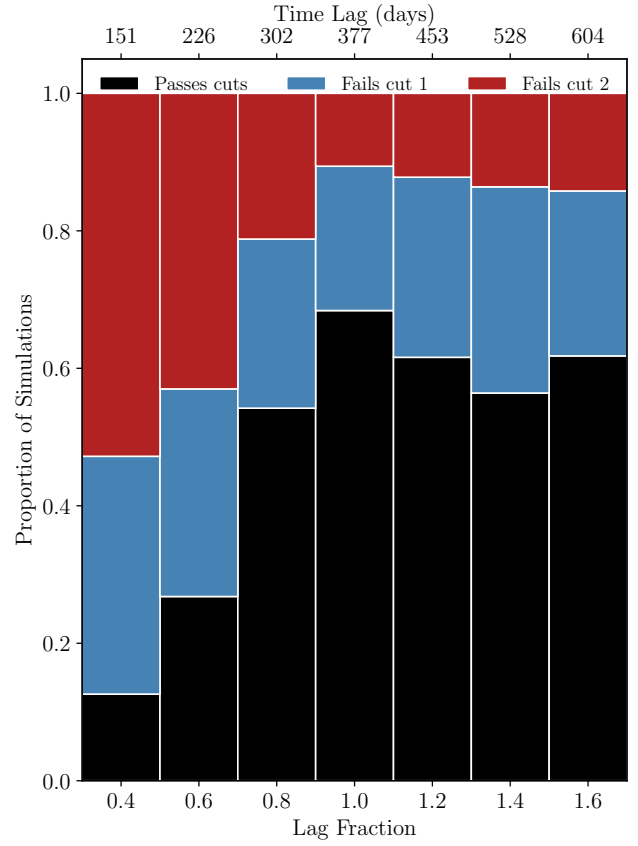


Figure 10. View of the effect of the quality cuts on the simulations for J0226-0459. This shows the proportion of lags in each lag bin that pass the first two quality cuts with the black showing those that pass both quality cuts, blue showing the simulations that have consistent JAVELIN and ICDF measurements but with uncertainties greater than 33% and red showing those that fail to recover consistent results.

the first two quality cuts but is inconsistent with the physical lag in the lightcurves.

We illustrate our quality criteria in the form of a workflow for the analysis of each set of lightcurves. This workflow is depicted in Figure 13.

False positive cuts of 5% and 20% were chosen based on how likely a certain false positive rate should happen by chance. We have simulated lags in seven bins, so statistically some of the sources in the six other bins will scatter into the measured bin. If $\sim 1\%$ of the simulated lags are 3σ discrepant from their true value (as should be expected), then we would find up to a $\sim 5\%$ false positive rate. If $\sim 5\%$ of the simulated lags are 3σ discrepant from their true value (more than expected), then we would find up to a $\sim 20\%$ false positive rate.

5 APPLICATION TO OBSERVATIONAL DATA

In Sections 3 and 4 we developed the tools necessary to create a workflow that will result in not only accurate time lag measurements, but also the ability to assign a confidence in each measurement. This confidence can be used to construct relations out of only the high quality measurements, while informing us on the sources that would benefit from the constraining power of more data. In this

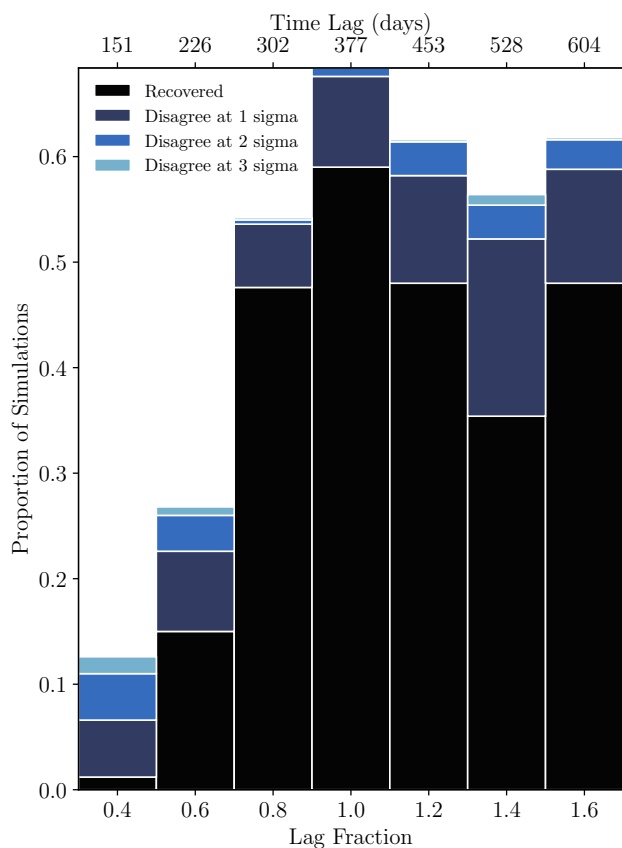


Figure 11. Accuracy of lag recovery as a function of input lag for J0226-0459. Black area shows the number of simulations in each bin that are accurate to within 1σ , with the lighter tones denoting those consistent within 2σ , 3σ with the lightest tone discrepant at a 3σ level. This gives a proxy for the recoverability of the source at different lags. For example if the true lag for this source is < 200 days it is unlikely that the lag would be recovered accurately even after passing the first two quality cuts.

pipeline we use the peak value of the posterior lag distribution as opposed to the median value as the peak value both avoids biases and improves the average performance of both ICCF and JAVELIN. In combination with this, we utilise the mean absolute deviation to compute the uncertainties in the lag measurements. Though our analysis found that this method can often overestimate the size of the uncertainties, this is likely more robust than consistently underestimating the uncertainties.

Of the six sources that we adopted as the test sample for this work, all passed the first selection criteria. This means that for all six JAVELIN and ICCF detected the same lag within 1σ . However, only two pass the second quality cut. In these instances the uncertainties range from 49% - 140%, not meeting the 33% maximum threshold for this criterion. For the remaining two sources, we have run a set of 3500 simulations at 7 different input lags, centered around the measured lag. This is an increase from the 200 per lag that was used in the Section 3. This was done in an effort to get a more well constrained false positive rate. From these simulations we can measure the recoverability at a range of different lags and determine the likelihood that the measured lag is a false positive. Using the definition of false positive rate that is described in Section 4, both of the sources that pass the previous quality cuts exhibit FPR $< 5\%$, with 3.4% and 4.9%, giving them both a quality 1 rating. There are

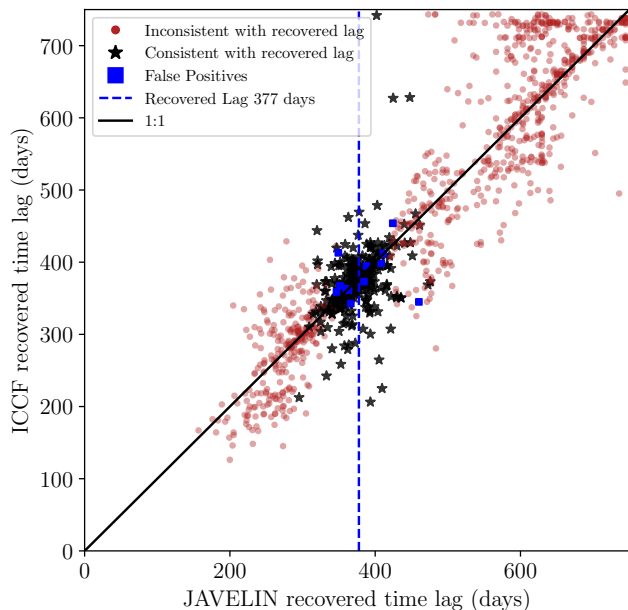


Figure 12. Graphical representation of the false positive test conducted on J0226-0459. The points on the plot represent all of the points that pass the first two quality cuts. We choose only the points that are consistent with the recovered lag in the data at a 1σ level, these are shown in black. The black stars show the points with an input lag consistent with the recovered lag. On the other hand the blue points show the simulations where the recovered lag is consistent with the lag recovered in the real data when the input to that simulation more than 3σ away from the point. From these we define our false positive rate as the number of blue points as a percentage of the number of blue and black combined.

no quality 2 or 3 sources in this sample. This is not too surprising as we expect that a large proportion of the sources that pass the first two quality cuts will be high standard with accompanying low FPR.

Previous studies (e.g. [Grier et al. 2019](#)) have used other definitions of the false positive rates. One of these considers how often negative lags are recovered in a large sample when the prior on the lag allows this. Since we are only considering a very small sample in this work, this approach would not be appropriate. There is also an approach wherein uncorrelated lightcurves are used to estimate how often a secure lag is discovered where a signal does not exist ([Shen et al. 2016](#)). We believe that the methodology described in this work will remove many of the false positives that would be highlighted by this method. To test this, 3500 uncorrelated lightcurves were produced with the same cadence and S/N as the two sources that passed the tests above. After performing lag recovery for these lightcurves with both ICCF and JAVELIN the results were analysed and cut using those defined in Section 4. Of the realisations that pass these cuts, we find the number that recover lags that are within a 1σ confidence of our recovered lag. For both of these sources we find a rate of $< 1\%$. This illustrates that the analysis pipeline developed in this work is effective in removing uncorrelated signals, a similar analysis performed in [Homayouni et al. \(2020\)](#) yielded a rate of $\sim 10\%$. This also shows that the false positive rate that is defined in Section 4.3 is a more representative measure of the false positive rate. With this in mind, combining all of the above work we arrive at the results shown in Table 3.

The results from our two quality 1 sources were also considered as part of an R-L relation. When added to an existing relation

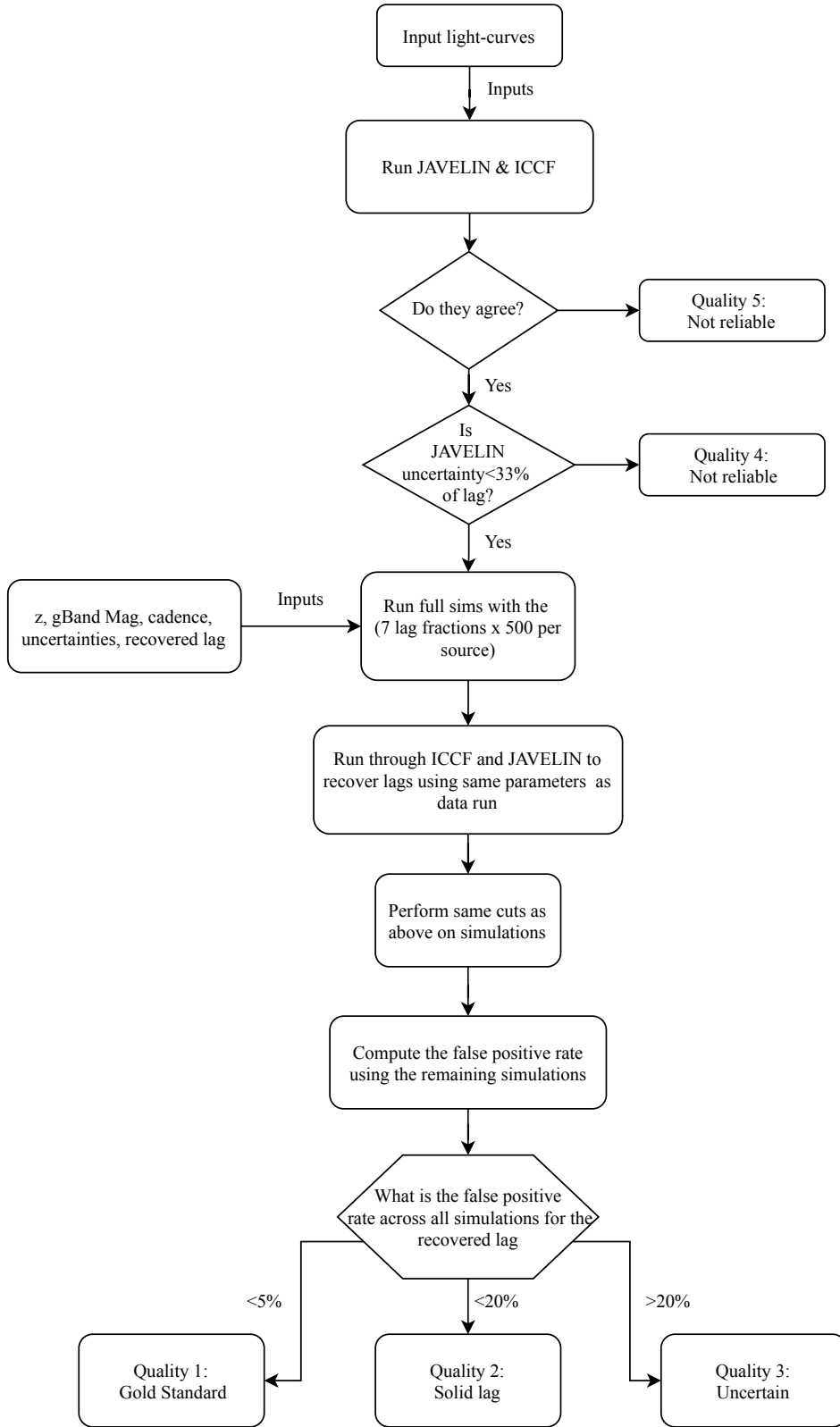


Figure 13. Flow of reverberation mapping pipeline. All sources are analysed using JAVELIN and ICCF. If the recovered lags disagree at a 1σ level, the source is rejected and given a quality rating of 5. If the uncertainty present in the any of the remaining sources is greater than 33% than those sources are cut and given a quality rating of 4. A set of 3500 simulations at 7 different input lags are run using the physical and observational parameters associated with each individual source. From these simulations a false positive rate is computed using the methods described in Section 4.3, this determines the final quality of these sources.

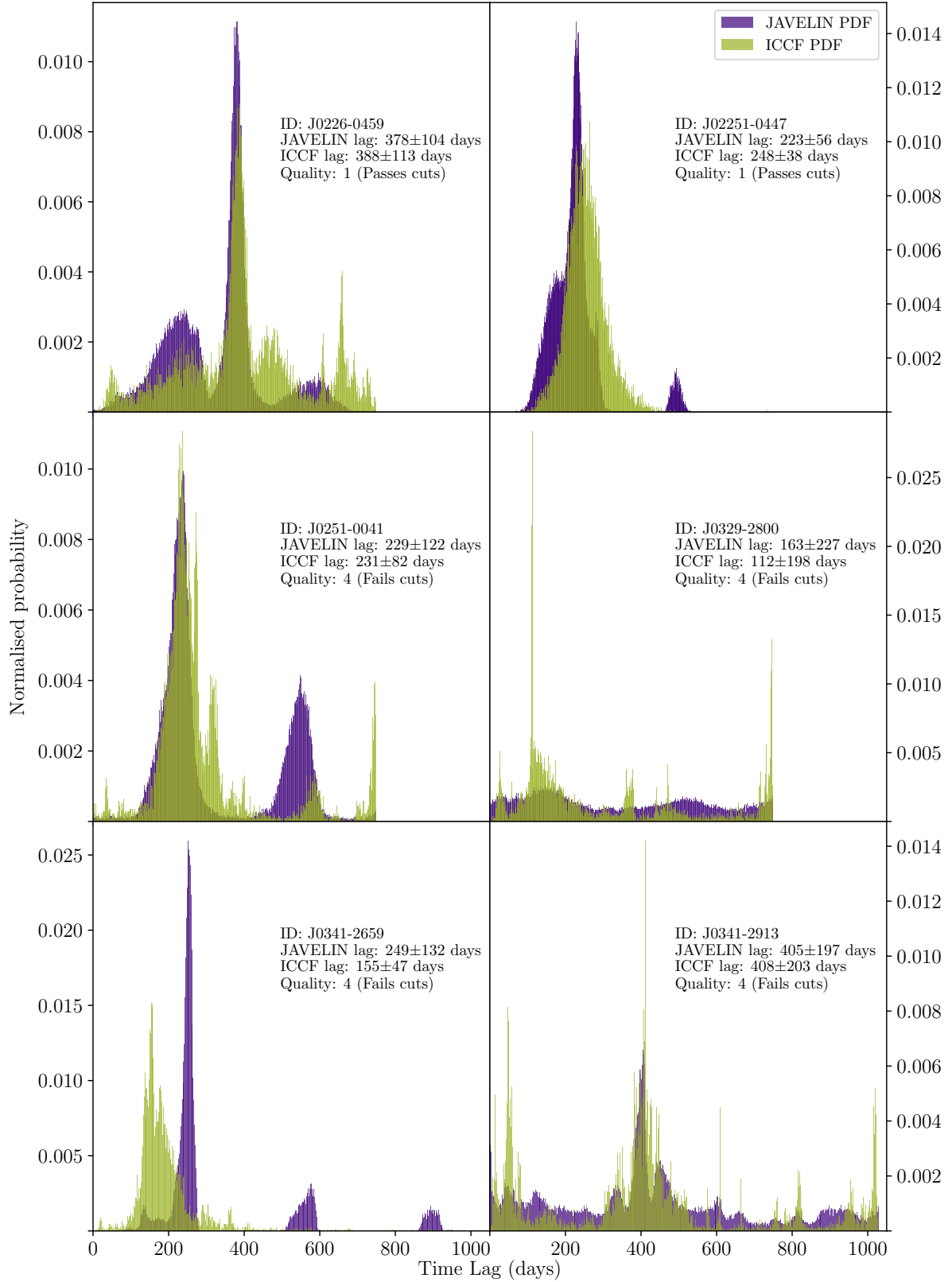


Figure 14. Full posterior lag distributions for both JAVELIN and ICCF for all six sources. The JAVELIN lag distribution contains 75000 iterations while the ICCF distribution contains 10000. The top two sources are those that pass the quality cuts and receive a quality 1 rating. In these there is very well defined peak and strong agreement between ICCF and JAVELIN. Of the remaining four PDFs, J0251-0041 (middle left) displays strong correlation between ICCF and JAVELIN, however, there is a large secondary peak produced by JAVELIN that inflates the uncertainties. This peak is likely due to aliasing, and may improve to a higher quality rating if an alias removal scheme was applied.

Table 3. Results from full analysis. Two of the sources pass all quality cuts and return a quality 1 rating with the remaining four receiving ratings of quality 4 as they failed to pass the second cut (uncertainties $> 33\%$).

ID	JAVELIN		ICCF		FPR (%)	Quality
	Lag (days)	Uncertainty (days)	Lag (days)	Uncertainty (days)		
J0225-0447	223	56	248	38	3.4	1
J0226-0459	378	104	388	113	4.9	1
J0341-2659	249	132	155	47	N/A	4
J0341-2913	405	197	408	203	N/A	4
J0329-2800	163	227	112	198	N/A	4
J0251-0041	229	122	231	82	N/A	4

containing a collection of gold standard C IV recoveries (Hoormann et al. 2019; Grier et al. 2019), they were found to be consistent and made no appreciable effect on the slope of the existing R-L relations in literature (Grier et al. 2019).

6 SUMMARY

In this paper we have developed an extensive set of simulations that can be used to model individual sources based on their exact variability, cadence and other physical traits. We use this powerful tool to quantify the lag recovery of each AGN in our sample rather than derive summary results from a population. Using these simulations with a set of six diverse AGN from the DES/OzDES sample we investigated how best to extract a time lag from the posterior lag distribution produced by JAVELIN and ICCF. We found that the peak of this distribution is the best measure of the time lag and the mean absolute deviation is the best measure of the uncertainty. From there we developed a set of quality cuts to show which of the recoveries would exhibit the characteristics of a reliable time lag. We cut any sources when ICCF and JAVELIN disagreed on the lag at more than 1σ , and also cut any sources whose uncertainties were large enough to include a lag of zero days at the 3σ level. Using a set of simulations specific to each source, we developed a false positive test that quantifies the likelihood that the recovered lag has been measured in an incorrect location. Using all of this analysis, the six test sources were processed through the newly developed pipeline to recover time lags and quality ratings. Of the six sources, two sources (J02251-0447, J02262-0459) were found to be in our highest quality category (quality 1) standard at lags of 223 ± 56 and 378 ± 104 days respectively.

In future work we aim to make improvements to several aspects of our analysis and reduction.

- Where in this paper we estimated the spectroscopic calibration uncertainties using the method described in Hoormann et al. (2019), we are developing a new empirical model of estimating the calibration uncertainties based on the F-star spectra for the upcoming OzDES papers. This new model would change the single-epoch uncertainties in the emission line lightcurves. However, our simulation tool allows statistical analysis with any input lightcurve uncertainties.

- While we have a false positive test for JAVELIN, there is not an in-depth analysis of false positives in ICCF. We have developed a test that correlates the height of the peak ICCF correlation with an effective p-value which could be used as another quality cut. This analysis was not considered in this work due to computational

limitations. Details for this method can be found in Appendix B.

- The photometry used in this analysis was measured in the g -band, however, we also have r - and i -band magnitudes. These are currently used only in our spectrophotometric calibration but it is possible that they could be used in constraining time lags as well. Using JAVELIN it is possible to cross-correlate multiple photometric bands as well as the spectroscopic lightcurve, in theory this would provide better constraints. The slight time-delay between the photometric bands due to the continuum emission from the host black hole's accretion disk (Mudd et al. 2018), would provide slightly different time domain information and may reduce effects such as aliasing. This method would be computationally expensive and thus was not explored here but is a consideration moving forward.

With a well understood set of criteria to help understand our confidence in measurements made on the full DES/OzDES sample, we now have a strong framework on which to build the bulk analysis of the remainder of the data set (Penton et al. in prep, Malik et al. in prep, Yu et al. in prep).

ACKNOWLEDGEMENTS

This research was supported in part by the Australian Government through the Australian Research Council Laureate Fellowship funding scheme (project FL180100168).

AP and UM are supported by the Australian Government Research Training Program (RTP) Scholarship.

PM and ZY were supported in part by the United States National Science Foundation under Grant No. 161553.

Funding for the DES Projects has been provided by the U.S. Department of Energy, the U.S. National Science Foundation, the Ministry of Science and Education of Spain, the Science and Technology Facilities Council of the United Kingdom, the Higher Education Funding Council for England, the National Center for Supercomputing Applications at the University of Illinois at Urbana-Champaign, the Kavli Institute of Cosmological Physics at the University of Chicago, the Center for Cosmology and Astro-Particle Physics at the Ohio State University, the Mitchell Institute for Fundamental Physics and Astronomy at Texas A&M University, Financiadora de Estudos e Projetos, Fundação Carlos Chagas Filho de Amparo à Pesquisa do Estado do Rio de Janeiro, Conselho Nacional de Desenvolvimento Científico e Tecnológico and the Ministério da Ciência, Tecnologia e Inovação, the Deutsche Forschungsgemeinschaft and the Collaborating Institutions in the Dark Energy Survey.

The Collaborating Institutions are Argonne National Laboratory, the University of California at Santa Cruz, the University of

Cambridge, Centro de Investigaciones Energéticas, Medioambientales y Tecnológicas-Madrid, the University of Chicago, University College London, the DES-Brazil Consortium, the University of Edinburgh, the Eidgenössische Technische Hochschule (ETH) Zürich, Fermi National Accelerator Laboratory, the University of Illinois at Urbana-Champaign, the Institut de Ciències de l’Espai (IEEC/CSIC), the Institut de Física d’Altes Energies, Lawrence Berkeley National Laboratory, the Ludwig-Maximilians Universität München and the associated Excellence Cluster Universe, the University of Michigan, NFS’s NOIRLab, the University of Nottingham, The Ohio State University, the University of Pennsylvania, the University of Portsmouth, SLAC National Accelerator Laboratory, Stanford University, the University of Sussex, Texas A&M University, and the OzDES Membership Consortium. Based in part on observations at Cerro Tololo Inter-American Observatory at NSF’s NOIRLab (NOIRLab Prop. ID 2012B-0001; PI: J. Frieman), which is managed by the Association of Universities for Research in Astronomy (AURA) under a cooperative agreement with the National Science Foundation.

The DES data management system is supported by the National Science Foundation under Grant Numbers AST-1138766 and AST-1536171. The DES participants from Spanish institutions are partially supported by MICINN under grants ESP2017-89838, PGC2018-094773, PGC2018-102021, SEV-2016-0588, SEV-2016-0597, and MDM-2015-0509, some of which include ERDF funds from the European Union. IFAE is partially funded by the CERCA program of the Generalitat de Catalunya. Research leading to these results has received funding from the European Research Council under the European Union’s Seventh Framework Program (FP7/2007-2013) including ERC grant agreements 240672, 291329, and 306478. We acknowledge support from the Brazilian Instituto Nacional de Ciência e Tecnologia (INCT) do e-Universo (CNPq grant 465376/2014-2).

This manuscript has been authored by Fermi Research Alliance, LLC under Contract No. DE-AC02-07CH11359 with the U.S. Department of Energy, Office of Science, Office of High Energy Physics.

DATA AVAILABILITY

The data underlying this article are available in DES data release 2, at <https://des.ncsa.illinois.edu/releases/dr2> and the OzDES data release 2 at <https://datacentral.org.au/services/download/>. The datasets were derived from sources in the public domain [Abbott et al. \(2021\)](#); [Lidman et al. \(2020\)](#).

REFERENCES

- Abbott T. M. C., et al., 2021, arXiv e-prints, p. [arXiv:2101.05765](https://arxiv.org/abs/2101.05765)
- Barth A. J., et al., 2011, *ApJ*, **743**, L4
- Bentz M. C., Katz S., 2015, *PASP*, **127**, 67
- Bentz M. C., Peterson B. M., Pogge R. W., Vestergaard M., Onken C. A., 2006, *ApJ*, **644**, 133
- Bentz M. C., Peterson B. M., Netzer H., Pogge R. W., Vestergaard M., 2009a, *ApJ*, **697**, 160
- Bentz M. C., et al., 2009b, *ApJ*, **705**, 199
- Blandford R. D., McKee C. F., 1982, *ApJ*, **255**, 419
- Childress M. J., et al., 2017, *MNRAS*, **472**, 273
- Dark Energy Survey Collaboration et al., 2016, *MNRAS*, **460**, 1270
- Denney K. D., et al., 2010, *ApJ*, **721**, 715
- Event Horizon Telescope Collaboration et al., 2019, *ApJ*, **875**, L6
- Fausnaugh M. M., et al., 2016, *ApJ*, **821**, 56
- Gaskell C. M., Peterson B. M., 1987, *ApJS*, **65**, 1
- Gebhardt K., et al., 2000, *ApJ*, **543**, L5
- Gebhardt K., Adams J., Richstone D., Lauer T. R., Faber S. M., Gültekin K., Murphy J., Tremaine S., 2011, *ApJ*, **729**, 119
- Greene J. E., et al., 2010, *ApJ*, **721**, 26
- Grier C. J., et al., 2012, *ApJ*, **755**, 60
- Grier C. J., et al., 2017, *ApJ*, **851**, 21
- Grier C. J., et al., 2019, *ApJ*, **887**, 38
- Homayouni Y., et al., 2020, *ApJ*, **901**, 55
- Hoormann J. K., et al., 2019, *MNRAS*, **487**, 3650
- Kaspi S., Smith P. S., Netzer H., Maoz D., Jannuzi B. T., Giveon U., 2000, *ApJ*, **533**, 631
- Kaspi S., Brandt W. N., Maoz D., Netzer H., Schneider D. P., Shemmer O., 2007, *ApJ*, **659**, 997
- Kelly B. C., Bechtold J., Siemiginowska A., 2009, *ApJ*, **698**, 895
- King A. L., et al., 2015, *MNRAS*, **453**, 1701
- Kozłowski S., et al., 2010, *ApJ*, **708**, 927
- Kuo C. Y., et al., 2011, *ApJ*, **727**, 20
- Li I-Hsiu J., et al., 2019, *ApJ*, **884**, 119
- Lidman C., et al., 2020, *MNRAS*, **496**, 19
- Lira P., et al., 2018, *ApJ*, **865**, 56
- MacLeod C. L., et al., 2010, *ApJ*, **721**, 1014
- Metzroth K. G., Onken C. A., Peterson B. M., 2006, *ApJ*, **647**, 901
- Mudd D., et al., 2018, *ApJ*, **862**, 123
- Neilsen Eric H. J., Annis J. T., Diehl H. T., Swanson M. E. C., D’Andrea C., Kent S., Drlica-Wagner A., 2019, arXiv e-prints, p. [arXiv:1912.06254](https://arxiv.org/abs/1912.06254)
- Onken C. A., Peterson B. M., 2002, *ApJ*, **572**, 746
- Peterson B. M., 1993, *PASP*, **105**, 247
- Peterson B. M., 2001, in Aretxaga I., Kunth D., Mújica R., eds, *Advanced Lectures on the Starburst-AGN*. p. 3 ([arXiv:astro-ph/0109495](https://arxiv.org/abs/astro-ph/0109495)), doi:[10.1142/9789812811318_0002](https://doi.org/10.1142/9789812811318_0002)
- Peterson B. M., Wanders I., Horne K., Collier S., Alexander T., Kaspi S., Maoz D., 1998, *PASP*, **110**, 660
- Peterson B. M., et al., 2004, *ApJ*, **613**, 682
- Peterson B. M., et al., 2005, *ApJ*, **632**, 799
- Shen Y., et al., 2011, *ApJS*, **194**, 45
- Shen Y., et al., 2015, *ApJS*, **216**, 4
- Shen Y., et al., 2016, *ApJ*, **818**, 30
- Shen Y., et al., 2019, *ApJ*, **883**, L14
- Starkey D. A., Horne K., Villforth C., 2016, *MNRAS*, **456**, 1960
- Trakhtenbrot B., Netzer H., 2012, *MNRAS*, **427**, 3081
- Trevese D., Perna M., Vagnetti F., Saturni F. G., Dadina M., 2014, *ApJ*, **795**, 164
- Vestergaard M., Peterson B. M., 2006, *ApJ*, **641**, 689
- Yu Z., Kochanek C. S., Peterson B. M., Zu Y., Brandt W. N., Cackett E. M., Fausnaugh M. M., McHardy I. M., 2020, *MNRAS*, **491**, 6045
- Yuan F., et al., 2015, *MNRAS*, **452**, 3047
- Zu Y., Kochanek C. S., Peterson B. M., 2011, *ApJ*, **735**, 80
- Zu Y., Kochanek C. S., Kozłowski S., Udalski A., 2013, *ApJ*, **765**, 106

¹ School of Mathematics and Physics, University of Queensland, Brisbane, QLD 4072, Australia

² The Research School of Astronomy and Astrophysics, Australian National University, ACT 2601, Australia

³ Center for Cosmology and Astro-Particle Physics, The Ohio State University, Columbus, OH 43210, USA

⁴ Department of Astronomy, The Ohio State University, Columbus, OH 43210, USA

⁵ Radcliffe Institute for Advanced Study, Harvard University, Cambridge, MA 02138

⁶ Centre for Gravitational Astrophysics, College of Science, The Australian National University, ACT 2601, Australia

⁷ Departamento de Física Matemática, Instituto de Física, Universidade de São Paulo, CP 66318, São Paulo, SP, 05314-970, Brazil

⁸ Laboratório Interinstitucional de e-Astronomia - LIneA, Rua Gal. José Cristino 77, Rio de Janeiro, RJ - 20921-400, Brazil

- ⁹ Fermi National Accelerator Laboratory, P. O. Box 500, Batavia, IL 60510, USA
- ¹⁰ Centro de Investigaciones Energéticas, Medioambientales y Tecnológicas (CIEMAT), Madrid, Spain
- ¹¹ Institute of Cosmology and Gravitation, University of Portsmouth, Portsmouth, PO1 3FX, UK
- ¹² CNRS, UMR 7095, Institut d'Astrophysique de Paris, F-75014, Paris, France
- ¹³ Sorbonne Universités, UPMC Univ Paris 06, UMR 7095, Institut d'Astrophysique de Paris, F-75014, Paris, France
- ¹⁴ Department of Physics and Astronomy, Pevensey Building, University of Sussex, Brighton, BN1 9QH, UK
- ¹⁵ Department of Physics & Astronomy, University College London, Gower Street, London, WC1E 6BT, UK
- ¹⁶ Instituto de Astrofísica de Canarias, E-38205 La Laguna, Tenerife, Spain
- ¹⁷ INAF - Astronomical Observatory of Trieste, I-34143, Trieste, Italy
- ¹⁸ Center for Astrophysical Surveys, National Center for Supercomputing Applications, 1205 West Clark St., Urbana, IL 61801, USA
- ¹⁹ Department of Astronomy, University of Illinois at Urbana-Champaign, 1002 W. Green Street, Urbana, IL 61801, USA
- ²⁰ Institut de Física d'Altes Energies (IFAE), The Barcelona Institute of Science and Technology, Campus UAB, 08193 Bellaterra (Barcelona) Spain
- ²¹ INAF-Osservatorio Astronomico di Trieste, via G. B. Tiepolo 11, I-34143 Trieste, Italy
- ²² Institute for Fundamental Physics of the Universe, Via Beirut 2, 34014 Trieste, Italy
- ²³ Observatório Nacional, Rua Gal. José Cristino 77, Rio de Janeiro, RJ - 20921-400, Brazil
- ²⁴ Department of Physics, University of Michigan, Ann Arbor, MI 48109, USA
- ²⁵ Department of Astronomy/Steward Observatory, University of Arizona, 933 North Cherry Avenue, Tucson, AZ 85721-0065, USA
- ²⁶ Jet Propulsion Laboratory, California Institute of Technology, 4800 Oak Grove Dr., Pasadena, CA 91109, USA
- ²⁷ Santa Cruz Institute for Particle Physics, Santa Cruz, CA 95064, USA
- ²⁸ Institute of Theoretical Astrophysics, University of Oslo. P.O. Box 1029 Blindern, NO-0315 Oslo, Norway
- ²⁹ Institut d'Estudis Espacials de Catalunya (IEEC), 08034 Barcelona, Spain
- ³⁰ Institute of Space Sciences (ICE, CSIC), Campus UAB, Carrer de Can Magrans, s/n, 08193 Barcelona, Spain
- ³¹ Kavli Institute for Cosmological Physics, University of Chicago, Chicago, IL 60637, USA
- ³² Instituto de Física Teórica UAM/CSIC, Universidad Autónoma de Madrid, 28049 Madrid, Spain
- ³³ Department of Astronomy, University of Michigan, Ann Arbor, MI 48109, USA
- ³⁴ Department of Physics, Stanford University, 382 Via Pueblo Mall, Stanford, CA 94305, USA
- ³⁵ Kavli Institute for Particle Astrophysics & Cosmology, P. O. Box 2450, Stanford University, Stanford, CA 94305, USA
- ³⁶ SLAC National Accelerator Laboratory, Menlo Park, CA 94025, USA
- ³⁷ Department of Physics, The Ohio State University, Columbus, OH 43210, USA
- ³⁸ Center for Astrophysics | Harvard & Smithsonian, 60 Garden Street, Cambridge, MA 02138, USA

- ³⁹ Lawrence Berkeley National Laboratory, 1 Cyclotron Road, Berkeley, CA 94720, USA
- ⁴⁰ Australian Astronomical Optics, Macquarie University, North Ryde, NSW 2113, Australia
- ⁴¹ Lowell Observatory, 1400 Mars Hill Rd, Flagstaff, AZ 86001, USA
- ⁴² George P. and Cynthia Woods Mitchell Institute for Fundamental Physics and Astronomy, and Department of Physics and Astronomy, Texas A&M University, College Station, TX 77843, USA
- ⁴³ Institució Catalana de Recerca i Estudis Avançats, E-08010 Barcelona, Spain
- ⁴⁴ Physics Department, 2320 Chamberlin Hall, University of Wisconsin-Madison, 1150 University Avenue Madison, WI 53706-1390
- ⁴⁵ Université Clermont Auvergne, CNRS/IN2P3, LPC, F-63000 Clermont-Ferrand, France
- ⁴⁶ Institute of Astronomy, University of Cambridge, Madingley Road, Cambridge CB3 0HA, UK
- ⁴⁷ Department of Astrophysical Sciences, Princeton University, Peyton Hall, Princeton, NJ 08544, USA
- ⁴⁸ Department of Physics, Duke University Durham, NC 27708, USA
- ⁴⁹ School of Physics and Astronomy, University of Southampton, Southampton, SO17 1BJ, UK
- ⁵⁰ Computer Science and Mathematics Division, Oak Ridge National Laboratory, Oak Ridge, TN 37831
- ⁵¹ McDonald Observatory, The University of Texas at Austin, Fort Davis, TX 79734
- ⁵² Max Planck Institute for Extraterrestrial Physics, Giessenbachstrasse, 85748 Garching, Germany
- ⁵³ Universitäts-Sternwarte, Fakultät für Physik, Ludwig-Maximilians Universität München, Scheinerstr. 1, 81679 München, Germany

APPENDIX A: SIMULATION PARAMETERS

A1 Variability time-scale, τ_D , and amplitude, SF_∞

MacLeod et al. (2010) determined the following power-law relationship between τ_D and SF_∞ and the physical properties of AGN:

$$\log_{10}(\alpha) = A_\alpha + B_\alpha \log_{10} \left(\frac{\lambda}{4000} \right) + C_\alpha (M_i + 23) + D_\alpha \log_{10} \left(\frac{M_{\text{BH}}}{10^9 M_\odot} \right) \quad (\text{A1})$$

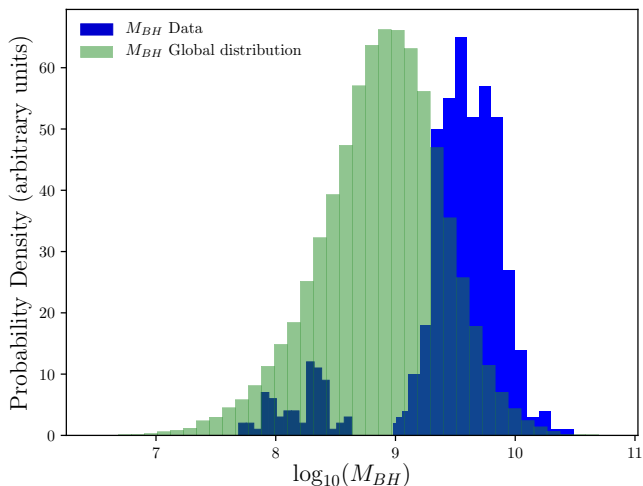
where α refers to τ_D (in days) or SF_∞ (in mag), λ (Å) is the rest-frame continuum wavelength, M_i is the absolute i -band magnitude of the source and M_{BH} is the mass of the black hole (in solar masses). The coefficients are given in Table A1. The correlations were found after converting timescales to the rest-frame of the sources, therefore the estimated τ_D values were multiplied by $(1+z)$ to create simulated light curves in the observed frame.

The black hole mass that is often used in simulations of this type is that predicted from the following Gaussian distribution used by MacLeod et al. (2010):

$$P(\log_{10} M_{\text{BH}} | M_i) = \frac{1}{\sqrt{2\pi\sigma_{M_{\text{BH}}}^2}} \exp \left[-\frac{(\log_{10} M_{\text{BH}} - \log_{10} \overline{M}_{\text{BH}})^2}{2\sigma_{M_{\text{BH}}}^2} \right] \quad (\text{A2})$$

Table A1. Coefficients of the power law relation defined for the damping timescale and structure function.

	τ_D	SF_∞
A	2.4	-0.51
B	0.17	-0.48
C	0.03	0.13
D	0.21	0.18

**Figure A1.** Histograms showing that our lag measurements primarily sample the high-mass end of the black hole mass distribution predicted by Equation A2. This is expected since we are primarily sensitive to long lags. The data in blue was obtained using the lag estimated from the $R - L$ relations listed in Table A2 and the line velocities from the RMS spectra for each source. These are then used to compute a mass using the virial relation (Equation 1). The green distribution is the prediction of the black hole mass distribution using Equation A2 and the absolute i -band magnitudes for each source.

with mean $\log_{10} \overline{M}_{\text{BH}} = 2.0 - 0.27M_i$ and standard deviation $\sigma_{M_{\text{BH}}} = 0.58 + 0.011M_i$ which signifies the dispersion in the black hole population.

In general, Equation A2 can be used to estimate the black hole masses for a large population of SMBH. However, it was found that, due to our survey target selection, the expected masses for our sources were tightly localised to much smaller regions than this distribution would predict.

Figure A1 shows the difference in distributions between the masses for the OzDES sample as predicted by Equation A2 in comparison with the distribution of these same black hole masses estimated using the virial relation (Equation 1). To use the virial relation we have used the $R - L$ relations from Table A2 to find an approximate radius of the BLR. Then used the RMS spectrum for each source to find the velocity of the region. The two distinct groups of blue in Figure A1 represent the $H\beta$ sources ($\sim 10^8 M_\odot$) and the C iv and Mg II sources ($\sim 10^9 - 10^{10.5} M_\odot$). The reason for the distinct groups is due to both survey design and astrophysical constraints. All of the nearby sources utilise the $H\beta$ line and are generally smaller/dimmer sources. This in general means that they host a lower mass SMBH. At a higher redshift we target much brighter objects, which generally house much larger SMBHs.

There are also simply no quasars that house ($> 10^9 M_\odot$) SMBH at $z < 0.6$ in our survey footprint. Due to these differences from the commonly accepted population distribution we conclude that the distributions in blue are much more likely to represent the physical characteristics of our sample. The BH mass that is used in our simulations is drawn randomly from these distributions, split into the appropriate emission line, as opposed to the global distribution from MacLeod et al. (2010) that is commonly used.

A2 Expected lag, τ

We estimated the rest-frame lag for each source using published $R - L$ relationships for each of the emission lines, which have the form:

$$\log_{10}(R) = K + \alpha \times \log_{10}(\lambda L_\lambda) \quad (\text{A3})$$

where R is the radius of the BLR in light-days (*i.e.*, the lag, τ , in days), L_λ is the monochromatic continuum luminosity at wavelength λ (\AA) in $\text{erg s}^{-1} \text{\AA}^{-1}$, K is the zero point for the relation, and α is the slope of the power law relationship. We use the $R - L$ relation calibrated for C iv from Hoormann et al. (2019). The coefficients of the $R - L$ relationship for each emission line are given in Table A2.

The simulated light curves were generated in the observed frame, so to generate the expected observe-frame lags for each source, the rest-frame lags were multiplied by $(1 + z)$.

APPENDIX B: NULL HYPOTHESIS TESTING

We apply the null hypothesis test to measure the confidence of ICCF results, as a potential addition to our significance criteria.

We randomised the spectroscopic light curves (shuffled flux values while keeping observation dates the same), and cross correlated this with the original photometric lightcurve. From the CCF, we found the value of the cross correlation coefficient at the peak of the CCF, r_{max} . After 100 iterations, the p -value was calculated as the proportion of the r_{max} values which exceeded the r_{max} of the CCF computed using the original pair of light curves.

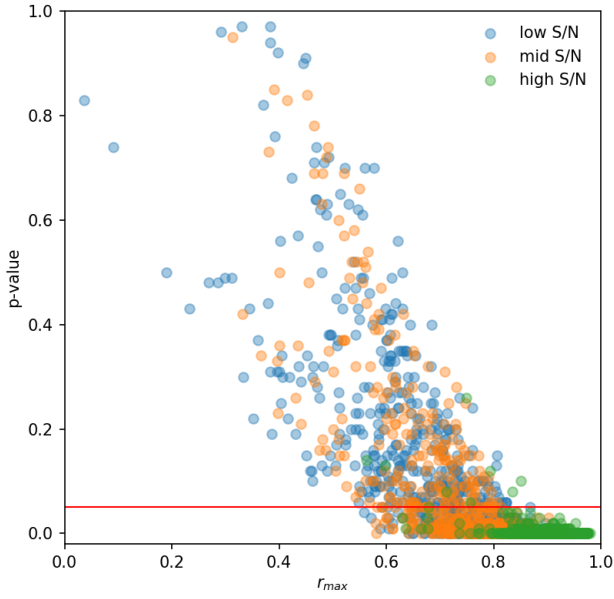
We chose to randomise the spectroscopic lightcurve, rather than using other lightcurve realisations for the same source. Other simulated lightcurve realisations have the same variability timescale and underlying lag as the source, and therefore may find significant spurious correlations at random lag values. If a purported uncorrelated lightcurve happened to have the same ‘increasing to decreasing slope’ feature, there would be correlation.

Our aim was to apply the null hypothesis test to our data, as an additional metric to quantify the reliability of lags recovered using the ICCF method. From our application of this test, the p -value tells us the proportion of uncorrelated light curves that are producing a correlation signal of the same strength or greater than that of our observed light curves. Therefore, we can use this p -value as a measure of confidence in the recovery from ICCF. We expect signal-to-noise to be the primary influencing factor here, as after randomising, the correlation would be ‘wiped-out’ most for the high S/N light curves.

Figure B1 shows the p -value for each of the 100 realisations for each lag fraction of the low, mid and high signal-to-noise sources. As we expected, the p -values for the high S/N sources are quite low, indicating confident recovery. We see that below a r_{max} of 0.5, there are always a significant number of uncorrelated signals which exceed this r_{max} , resulting in high p -values. Therefore we can not

Table A2. Radius-Luminosity ($R - L$) relationship coefficients for each emission-line (Eq. A3).

Line	K	α	λ (\AA)	Paper
H β	-21.2 ± 2.2	0.517 ± 0.033	5100	Bentz et al. (2009a)
Mg II	-25.72 ± 0.62	0.615 ± 0.014	3000	Trakhtenbrot & Netzer (2012)
C IV	-23.3 ± 2.6	0.55 ± 0.04	1350	Kaspi et al. (2007)

**Figure B1.** The p -value vs. r_{\max} for each of the 100 lightcurve realisations at the various input lags fractions. This is shown for each of the low, mid and high signal-to-noise sources. The r_{\max} is of the original pair of light curves. The red line indicates a p -value of 0.05, for reference.

trust a result which has a r_{\max} below 0.5. Above this, there is still a chance of having a high p -value, depending on the variability properties of the source.

We use the results of this test to propose additional criteria to strengthen our analysis pipeline. If the CCF of the original light curves has a $r_{\max} \leq 0.5$ the source should not proceed through the pipeline, as it has a weak correlation signal. We should apply the null hypothesis test to sources which pass this cut. If the p -value from this test is less than 0.1 we should proceed.

This paper has been typeset from a $\text{\TeX}/\text{\LaTeX}$ file prepared by the author.